Asian Journal of Pharmaceutical Sciences 17 (2022) 713–727

Available online at www.sciencedirect.com

ScienceDirect

journal homepage: www.elsevier.com/locate/AJPS

Original Research Paper

Lignin-assisted construction of sub-10 nm supramolecular self-assembly for photothermal immunotherapy and potentiating anti-PD-1 therapy against primary and distant breast tumors

Xudong Fan[a], *Tianxiang Yue*[a], *Aidi Liu*[a], *Xiaowei Xie*[a], *Weixiang Fang*[a], *Yinghui Wei*[a], *Hangsheng Zheng*[a], *Hongyue Zheng*[c], *Meiqi Zhou*[d], *Jigang Piao*[a,b,e,*], *Fanzhu Li*[a,b,*]

[a] *School of Pharmaceutical Sciences, Zhejiang Chinese Medical University, Hangzhou 310053, China*
[b] *Key Laboratory of Neuropharmacology and Translational Medicine of Zhejiang Province, School of Pharmaceutical Sciences, Zhejiang Chinese Medical University, Hangzhou 310053, China*
[c] *Libraries of Zhejiang Chinese Medical University, Zhejiang Chinese Medical University, Hangzhou 310053, China*
[d] *Department of Breast Surgery, Key Laboratory of Cancer Prevention and Intervention, China National Ministry of Education, Second Hospital of Zhejiang, University College of Medicine, Hangzhou 310009, China*
[e] *Academy of Chinese Medical Sciences, Zhejiang Chinese Medical University, Hangzhou 310053, China*

ARTICLE INFO

Article history:
Received 24 February 2022
Revised 28 May 2022
Accepted 11 July 2022
Available online 29 July 2022

Keywords:
Lignin
Supramolecular self-assembly
Photothermal-immunotherapy
Anti-PD-1

ABSTRACT

Photothermal therapy (PTT) has brought hope for cancer treatments, with hyperthermia-induced immunogenic cell death (ICD), which is a critical part of therapeutically induced antitumor immune responses. Limited immune stimulation response in PTT is the primary reason for incomplete tumor ablation, therefore demonstrating urgent requirements for ICD amplifier. Herein, a sub-10 nm supramolecular nanoassembly was formed by co-assembly of clinically approved aluminum adjuvant and commonly used indocyanine green (ICG) under the assistance of lignosulfonate (LS, a green and sustainable multifunctional lignin derivative) for localized photothermal-immunotherapy of breast cancer. The overall results revealed that LS-Al-ICG is capable of inducing amplified ICD, efficiently eliciting solid immune responses through dendritic cells (DCs) activation and cytotoxic T-cell responses initiation for tumor killing. Moreover, anti-PD-1 therapy blocked the PD-1 pathway and led to remarkable anti-tumor efficacy against laser-irradiated primary tumors and distant tumors by potentiating systemic tumor specific T cell immunity. The results of this study demonstrate a handy and extensible approach for engineering green natural lignin nanoparticles for cancer immunotherapy, which shows promise for delivering other therapeutics in biomedical applications.

* Corresponding authors.
E-mail addresses: jgpiao@zcmu.edu.cn (J.G. Piao), lifanzhu@zcmu.edu.cn (F.Z. Li).
Peer review under responsibility of Shenyang Pharmaceutical University.

https://doi.org/10.1016/j.ajps.2022.07.002

1. Introduction

Immunogenic cell death (ICD) is attracting worldwide attention because it enables dying cancer cells to modulate the host's anti-tumor immune system and stimulate immune surveillance [1]. Therefore, effective activation of treatment-induced ICD is clinically important for raising systemic anti-tumor immunity and eradicating post-treatment/abscopal cancer tissues [2,3]. Among various strategies used for ICD induction, photothermal therapy (PTT) represents a non-invasive modality, where cancer cells are ablated owing to localized heat generated by photothermal agents following the irradiation of near-infrared (NIR) [4–7]. It has been well established that PTT can elicit ICD by inducing the release of tumor-associated antigens (TAAs) and damage-associated molecular patterns (DAMPs), such as calreticulin (CRT) translocation, exodus of high mobility group box 1 protein (HMGB1) expression, and adenosine triphosphate (ATP) leakage [8,9]. These molecules facilitate the immunogenic processes of antigen-presenting cells (APCs), as well as the subsequent recruitment and maturation of dendritic cells (DCs), which promotes pro-inflammatory cytokine secretion and stimulates cytotoxic T lymphocytes (CTLs) [10,11]. Although PTT can rapidly shrink tumor volumes, in general, it is hard to completely eliminate tumors by using PTT treatment alone due to a limited penetration depth and short-term immune system stimulation [12,13]. However, combining PTT with immunotherapy is expected to overcome the above challenges [4,14].

Recent research on using immunomodulation to enhance therapeutic efficacy has led to enormous progress in immunoadjuvants, which are immunostimulatory molecules that enhance or induce the function of cellular immune response [15,16]. At present, immunoadjuvants are frequently employed in combination with PTT for addressing the problem of limited immune stimulation [17–19]. In conjunction with immunoadjuvants, PTT-induced DAMPs and TAAs can take shape *in situ* vaccines, which can obtain excellent immune efficacy through priming intense immune responses [20]. Immunological effects have been demonstrated for different types of immunoadjuvants, for example, inorganic adjuvants, organic adjuvants, synthetic adjuvants and oil et al. [15]. Aluminum adjuvants is the most widely used adjuvant in human vaccine so far, which has shown acceptable safety and effectiveness in the marketed vaccines [21,22]. However, weak cell-mediated immune stimulation limits the clinical use of aluminum adjuvant, which can be enhanced by means of nano preparation [23,24]. Recently, numerous experimental efforts have been devoted to enhance aluminum ajduvant-based therapeutic treatments in combination with PTT. For example, Chen et al. prepared a multifunctional nanosystem of polydopamine-coated Al_2O_3 nanoparticles (pD-Al_2O_3 NPs), together with co-administered CpG for photothermal immunotherapy [25]. Zhu et al. designed the classical aluminum adjuvants and the photosensitizer chlorin e6 (Ce6) into bovine serum albumin (BSA) *via* biomineralized method for photo-mediated immune therapy [26]. Therefore, combination therapies involving NP-based photothermal agents and aluminum adjuvants are promising approaches to activating the body's immune system.

So far, numerous strategies have been ultilized in construction of theranostic nanomedicines [27,28]. Metal-coordinated supramolecular nanoassemblies (MCSN), which form nanoscopic architectures driven by non-covalent interactions and therefore have structures and functions beyond those of the individual molecular components, have received substantial interest for cancer theranostics. Benefiting from the distinctive physicochemical properties, MCSN can bridge the boundaries between traditional inorganic and organic materials [29–31]. Facile engineering can also be achieved by functional components adjustion. When selecting organic biomaterials, it is worth noting that lignin is the second most abundant natural polymer after cellulose, while has not yet been fully utilized for conversion into high-value products [32,33]. Lignosulfonate (LS), a water-soluble derivative of lignin, is the major by-product of sulfite pulping approach. Because of its low cost, all-natural biodegradability, non-toxicity, and complexation properties, LS has greater potentials for drug delivery and cancer therapy than proteins and other polymers [34,35]. Previously, we found that LS nanocomposites can be synthesized with various morphologies in media with different pH values [36]. Moreover, LS and gentamicin sulfate (GS) were shown to self-assemble into a nanocomposite (LS-GS), which exhibited excellent antibacterial and wound-healing activities [37]. LS has been used for several applications in the nanotechnology field, included the green synthesis of NPs [34,35]. Considering all of the attractive properties, LS may be an ideal candidate for fabricating aluminum MCSN.

In this study, we developed an innovative MCSN in association with anti-PD-1 treatment for photothermal immunotherapy against breast cancer (Fig. 1). In this approach, we used LS as a complexing agent, surfactant, and stabilizer, which subsequently co-assembled with the photosensitizer indocyanine green (ICG) and an aluminum adjuvant. The entire LS-Al-ICG nanosystem was stabilized by multiple intermolecular interactions, including hydrogen and coordination bonds. Additionally, our experimental results confirmed that LS-Al-ICG primarily accumulated in tumors and further degraded in the acidic tumor microenvironment. Under NIR laser irradiation, enhanced ICD induced by the photothermal effects of LS-Al-ICG. LS-Al-ICG stimulated cytokine release and antigen presentation, thereby potentiating DCs activation and subsequent tumor specific T cell immunity. Eventually, these primed tumor specific T cells attacked primary tumors after PTT treatment, as well as distant tumors following combination treatment with anti-PD-1 therapy. Taken together, our results show that the facile self-assembly process using naturally derived lignin to fabricate the supramolecular nanosystem combined with effective PTT and immunotherapy, and provide new ideas for the development of clinically effective treatment paradigm for breast cancer.

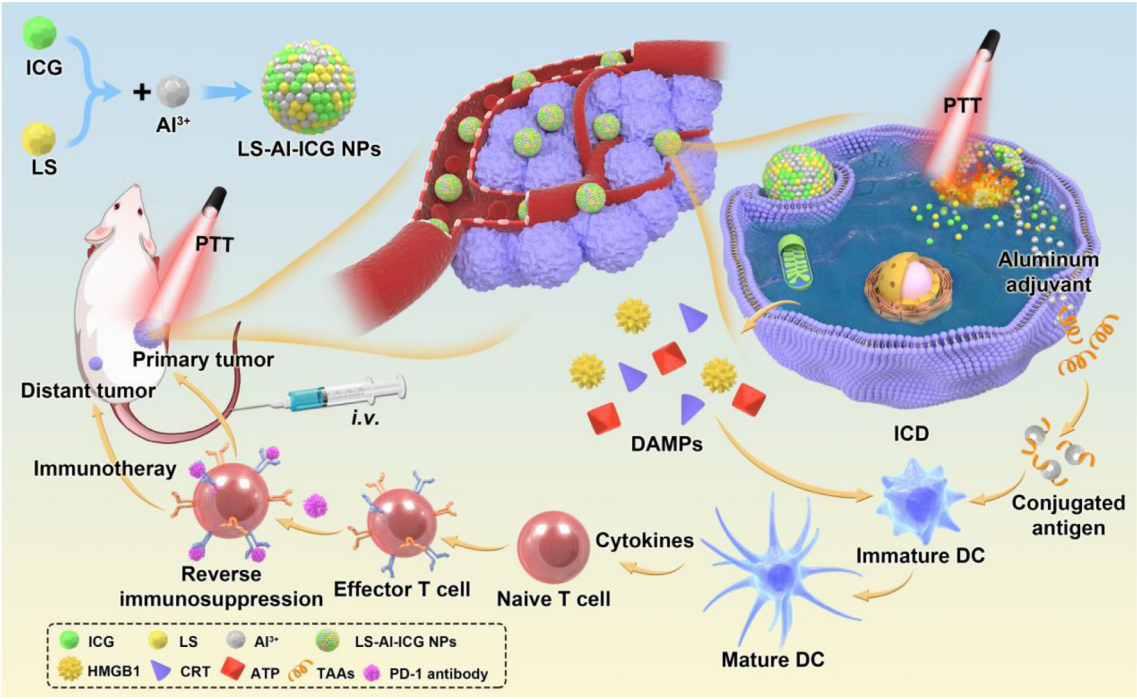

Fig. 1 – Schematic diagram of LS-Al-ICG for photothermal immunotherapy against primary and distant breast tumors.

2. Materials and methods

2.1. *Materials*

Calcium lignosulfonate (CLS) was acquired from Macklin. Aluminum chloride ($AlCl_3$) and ICG were bought from Aladdin. The Cell Counting Kit-8 (CCK-8) was bought from Biosharp. We obtained Alexa Fluor 488-labeled goat anti-rabbit IgG ($H+L$), 4,6-diamidino-2-phenylindole (DAPI), the ATP Assay Kit, rabbit monoclonal antibodies against CRT and HMGB1 from Beyotime. Enzyme-linked immunosorbent assay (ELISA) kits for detecting interleukin-2 (IL-2), tumor necrosis factor-α (TNF-α), and interferon-γ (IFN-γ) were purchased from Jiangsu Meimian Industrial Co., Ltd. PD-1 inhibitor was bought from BeiGene. Fluorochrome-labeled anti-mouse monoclonal antibodies (CD11c-allophycocyanin (APC), CD80-fluorescein isothiocyanate (FITC), CD86-phycoerythrin (PE), CD3-FITC, CD8a-PE, and CD4-APC) were bought from Proteintech.

2.2. *Synthesis of LS-AL-ICG*

LS-Al-ICG was synthesized using a one-step process. On the basis of the optimization studies, calcium lignosulfonate solution (3 mg/ml, 10 ml) was mixed with ICG solution (0.2 mg/ml, 5 ml) and stirred at 25 °C. Next, aluminum chloride solution (2 mg/ml, 15 ml) was added at a rate of 0.2 ml/min and mixture stirred overnight. Finally, LS-Al-ICG was collected through centrifugation (5000 rpm, 10 min) and dispersed in ultra-pure water.

2.3. *Characterization of LS-AL-ICG*

Morphology and elemental analyses of LS-Al-ICG were performed by transmission electron microscopy (TEM; JEM-F2100, Japan). The hydrodynamic diameter, zeta potential and polydispersity index (PDI) of the LS-Al-ICG were acquired using a Nano-ZS90 Zetasizer (Malvern Panalytical, UK). The absorbance spectra of LS, $AlCl_3$, ICG, and LS-Al-ICG was determined using an ultraviolet-visible near-infrared (UV–Vis-NIR) spectrometer (UV-3600, Japan). X-ray photoelectron spectroscopy (XPS) was used to analyze the LS-Al-ICG in terms of their elemental composition and chemical state, using a K-Alpha XPS instrument (Thermo Scientific, USA). Fourier transform infrared spectroscopy (FTIR, Thermo Scientific, USA) was used to collect infrared spectra, for which the samples were prepared using KBr.

2.4. *Stability of LS-AL-ICG*

The stability of LS-Al-ICG was studied according to the variations in mean particle size, zeta potential, and PDI, which were measured after storage in various buffers and the presence of serum at 4 °C over time.

2.5. *Encapsulation efficiency (EE) and drug-loading rate (DL) of LS-AL-ICG*

The EE and DL of LS-Al-ICG for ICG and Al were calculated using the Eq. 1 and Eq. 2 indicated below. The ICG concentration was assayed by UV–Vis-NIR spectrometer, whereas the Al concentration was assayed by inductively

coupled plasma (ICP; Thermo, ICAP 7400, USA)

$$\text{EE (\%)} = \frac{\text{Weight of ICG or Al in LS}-\text{Al}-\text{ICG}}{\text{Weight of ICG or Al added for the encapsulation step}} \times 100\% \quad (1)$$

$$\text{DL (\%)} = \frac{\text{Weight of ICG or Al in LS} - \text{Al} - \text{ICG}}{\text{Total LS} - \text{Al} - \text{ICG weight}} \times 100\% \quad (2)$$

2.6. Molecular docking of LS-AL-ICG

To explore the mechanism of LS-Al-ICG formation, we generated the structures of ICG, Al^{3+}, and CLS using the ChemDraw 3D and Gauss 5.0 software programs, and molecular docking was performed using Autodock.

2.7. Photothermal performance of LS-AL-ICG

The photothermal effect of LS-Al-ICG was evaluated by recording infrared images and temperature variation in condition of NIR laser irradiation (808 nm, 1 W/cm^2) with an infrared thermal camera (Testo 872; Testo SE & Co. KGaA, Germany). To study photothermal stability, temperature cycles were repeated 5 times. ICG and LS-Al-ICG (ICG: 20 μg/ml) were irradiated for 5 min, then paused for 10 min, cooled naturally to room temperature. The photothermal conversion efficiency (η) of the free ICG and LS-Al-ICG was calculated following Eq. 3 and Eq. 4:

$$\eta = \frac{\text{hS}\left(T_{max} - T_{surr}\right) - \text{hS}\left(T_{max.water} - T_{surr}\right)}{\text{P}\left(1 - 10^{-A}\right)} \quad (3)$$

where h and S represented the heat transfer coefficient and the surface area of the container. "T_{max}" "$T_{max.water}$" and "T_{surr}" were initial and the highest temperature of free ICG, LS-Al-ICG and water. "P" denoted the power of laser. "A" was the absorbance at 808 nm.

$$\text{hS} = \frac{\text{mc} + m'c'}{\tau} \quad (4)$$

"m" and "m′" were the mass of the solution containing ICG or LS-Al-ICG, and quartz dish, respectively. "c" and "c′" were the heat capacity of the water and quartz dish, respectively. Where "τ"was sample system time constant.

2.8. In vitro release study

To study ICG release, 0.5 ml LS-Al-ICG solution (ICG:260 μg/ml) were transferred to the dialysis membrane and submerged in 10 ml phosphate buffered saline (PBS), and shaken at 37 °C (pH = 5.0, 6.2 or 7.4). 1 ml PBS was removed dialysis membrane, then replaced with 1 ml primary PBS at indicated time points. The absorption at 780 nm in PBS was assayed using an UV–Vis-NIR spectrometer. The percentages of ICG release were calculated according to a standard curve.

2.9. Cell uptake in vitro

4T1 cells were seeded in laser confocal dishes (2×10^5 cells/well) and exposed for 4 h to free ICG or LS-Al-ICG (ICG: 16 μg/ml) in blank medium, followed by illumination or no illumination. The cellular uptake of LS-Al-ICG was observed by a confocal laser scanning microscope (CLSM; Olympus, Japan).

2.10. In vitro cytotoxicity assay

The cytotoxicity of LS-Al-ICG on human umbilical vein endothelial cells (HUVEC) was studied. HUVEC were cultured into 96-well plates (1×10^4 cells/well) and then incubated for 4 h with LS-Al-ICG at various concentrations (ICG: 0, 1, 2, 4, 8, or 16 μg/ml). Mouse 4T1 mammary carcinoma cells were seeded overnight in 96-well plates (1×10^4 cells/well), after which the cells were co-incubated with medium containing free ICG or LS-Al-ICG (ICG: 0, 1, 2, 4, 8, or 16 μg/ml) for 4 h. Next, replaced the drug containing medium with blank medium. The illuminated groups were treated with 808 nm laser for 5 min (1 W/cm^2). Cell viabilities were evaluated by performing CCK-8 assay.

2.11. Live/dead staining assay

4T1 cells cultured overnight in laser confocal dishes (5×10^5 cells/well), then cells were incubated with blank medium or medium containing LS-Al-ICG (ICG: 16 μg/ml) for 4 h. An 808 nm laser was used to irradiate the illuminated groups after washing with PBS. Additionally, mixed cells with propidium iodide (PI) and calcein-AM for 30 min, then observed under CLSM.

2.12. In vitro evaluation of DAMPs

4T1 cells (5×10^5 cells/well) were treated with blank medium or medium containing ICG or LS-Al-ICG (ICG: 16 μg/ml). After incubating for 4 h, the illuminated groups were subjected to 10-min laser irradaition, and then all groups were incubated with a monoclonal antibody against CRT or HMGB1 for 12 h at 4 °C. Subsequently, secondary antibody and DAPI were incubated with the cells. During the staining process, the cells were washed repeatedly with PBS. Ultimately, the fluorescent signals were observed under a CLSM. To measure ATP release, 4T1 cells were treated with blank medium or medium containing ICG or LS-Al-ICG (ICG: 16 μg/ml). After 4 h incubation, followed with or without illumination, the cell supernatants were collected by low-temperature centrifugation. ATP release into the culture supernatants was detected *via* the ATP assay kit.

2.13. In vitro DCs maturation

Bone marrow-derived dendritic cells (BMDCs) were isolated from BALB/c mice, seeded into Petri dishes (1×10^7 cells/10 ml RPMI 1640 medium with 10 ng/ml mouse GM-CSF). Nonadherent and loosely adherent immature BMDCs were collected on day 7 and then seeded into Petri dishes (1×10^6

cells/well). Culture supernatants from 4T1 cells subjected to different treatments (LS-Al-ICG ± NIR, ICG ± NIR, and control treatments) were added to BMDCs in Petri dishes. The BMDCs were collected after 24 h and stained with fluorochrome-labeled anti-mouse monoclonal antibodies (CD11c-APC, CD80-FITC, or CD86-PE) for 30 min and then analyzed by flow cytometry. IL-2, TNF-α, and IFN-γ production in culture supernatants were measured by performing ELISA.

2.14. *In vivo biodistributions*

Female BALB/c mice (6–8 weeks old) were obtained from the Laboratory Animal Center of Zhejiang Chinese Medical University. ICG or LS-Al-ICG (ICG: 4 mg/kg) were intraveneously administrated. To detect the ICG fluorescence signals, 4T1 tumor-bearing mice were anesthetized at the specified times (0.25, 0.5, 0.75, 1, 2, 4, 8 and 24 h) and imaged with an IVIS Spectrum Imaging System (Ex = 710 nm, Em = 745 nm). After 24 h, the major organs and tumor tissues were collected from the sacrificed mice for *ex vivo* tissue imaging.

2.15. *Anti-tumor effects evaluation*

The mice were injected with 4T1 cells subcutaneously on each side of the back in turn. After 14 d, when the volumes of the right tumor were close to 150 mm^3, the saline, free ICG, and LS-Al-ICG were intravenously injected into each group of mice, respectively. The illuminated groups were irradiated for 5 min with 808 nm laser (1 W/cm^2) on Days 1, 3 and 5. During this period, temperature elevations in the tumor sites were taken with an infrared thermal camera. Anti-PD-1 antibody was intravenously injected on Day 2, 4 and 6 (100 μg per mouse per injection). The mice were maintained in a controlled temperature and humidity environment with a regular light and dark cycle (12 h light, 12 h dark) and were given free food and water. Body weight and tumor volume were recorded every 2 d The survival time of mice was recorded from the beginning of treatment until Day 50. Tumor volumes were calculated using the Eq. 5:

$$\text{Volume}\left(mm^3\right) = \frac{\text{Length} \times \text{Width}^2}{2} \quad (5)$$

2.16. *Analysis of immune responses in vivo*

Each group of mice ($n = 3$) were sacrificed on the seventh day of treatment. Serum cytokine levels were measured using ELISA kits. Tumor-draining lymph nodes (TDLNs), primary tumors and spleens were dissected to prepare single-cell suspensions. To evaluate the maturity of DCs, lymphocytes were labeled with CD11c-APC, CD80-APC, and CD86-PE for flow cytometric analysis. Splenocytes stained with CD3-FITC, CD8a-PE, and CD4-APC were utilized to assess T cell activation.

2.17. *Histopathology examination*

Mice were sacrificed after a 21-d treatment cycle, and the tumor tissues and major organs were harvested and fixed in 10% paraformaldehyde for 1–2 d All tissues were dehydrated, embedded, and sectioned, after which H&E staining was performed with all tissues, and TUNEL assays were performed with tumor tissues. The tissues were investigated under a fluorescence microscope (Zeiss).

2.18. *Statistical analysis*

All experimental data were presented as the mean ± standard deviation (SD), with the sample size indicated. Groups were compared using SPSS software. P values of < 0.05 were considered to reflect statistically significant.

3. Results and discussion

3.1. *Preparation and characterization of LS-AL-ICG*

Here, we report the development of an innovative metal-coordinated supramolecular, self-assembling nanosystem for photothermal immunotherapy. The optimization results based on the hydrodynamic diameter, zeta potential, PDI, EE and DL for LS-Al-ICG were shown in Fig. S1 and S2. As illustrated in Fig. 2A, LS-Al-ICG formed through the co-assembly of CLS, ICG, and Al^{3+}. The morphology and size distribution of the prepared LS-Al-ICG was confirmed *via* TEM imaging (Fig. 2B). As visualized by the TEM images, the obtained LS-Al-ICG had a regular spherical morphology with an average diameter of 8.3 ± 2.0 nm and zeta potential of −20.7 ± 0.7 mV (Fig. 2C). Energy-dispersive X-ray spectroscopy (EDS) analysis showed that C, O, S, and Al elements existed in LS-Al-ICG with an atomic ratio of 69.0%, 28.1%, 1.6% and 1.3% (Fig. S3). The XPS spectra further verified the efficient loading of Al, which existed in a trivalent ionic state (Fig. S4). The DL and EE values of ICG and Al were next monitored spectrometrically because these parameters are critical for biomedical applications. The results showed that the EE values of ICG and Al were 35.70% ± 0.62% and 11.85% ± 0.45%, respectively. The DL values of ICG and Al were 7.10% ± 0.12% and 14.29% ± 0.54%, respectively (Fig. 2D-2E). Comparing the UV–Vis-NIR spectra of monomeric ICG with LS-Al-ICG revealed a broader Soret band and a red-shifted Q-band for the LS-Al-ICG with characteristic absorbance peak from 776 to 808 nm, suggesting that the LS-Al-ICG successfully self-assembled, which is beneficial for 808 nm laser-mediated photothermal conversion (Fig. 2F) [38].

To study the hydrogen bond assisted self-assembly, we performed Fourier transform infrared (FTIR) analysis of ICG, LS and LS-Al-ICG. As shown in Fig. S5, the corresponding characteristic bonds moved towards lower wavenumbers after self-assembly indicates the formation of hydrogen bonds. However, when LS-Al-ICG was stored in PBS (pH 5.0) for 24 h, the back-shifts of characteristic bands indicated the weakening of hydrogen bonds [39]. While the blueshift of the absorption peak of ICG (from 805 to 787 nm) in the UV–Vis-NIR spectrum confirms the weakening of π-π stacking interaction (Fig. S6) [40]. In addition, negligible changes in particle size, PDI and zeta potentials of LS-Al-ICG in PBS or DMEM with the presence of serum were observed during 7-d observation period (Fig. S7).

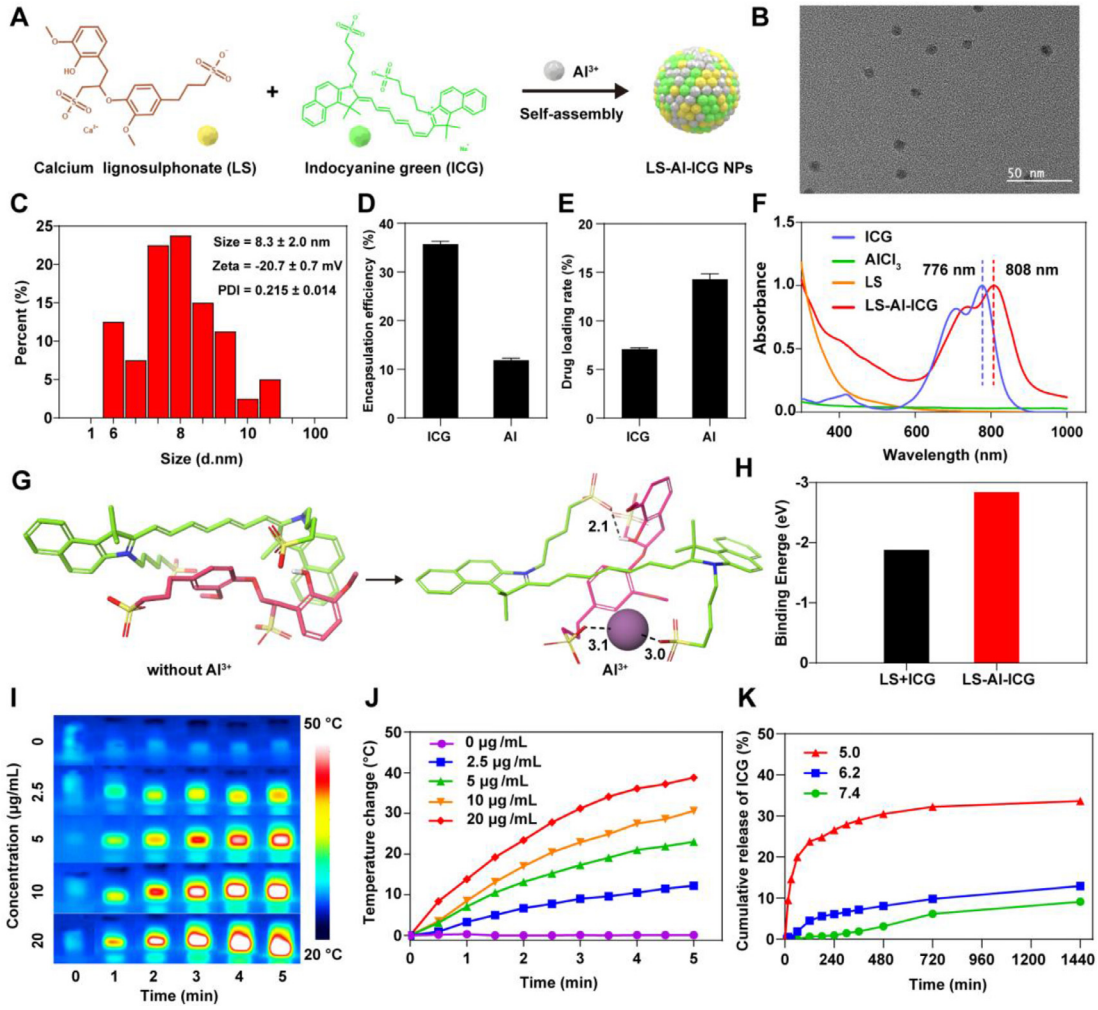

Fig. 2 – Characterization and *in vitro* release of LS-Al-ICG. (A) LS, ICG and Al^{3+} could self-assemble into uniform nanosized NPs. (B) TEM image of LS-Al-ICG. (C) Size distribution, zeta potential and PDI of LS-Al-ICG. (D-E) EE and DL of ICG and Al ($n = 3$, mean ± SD). (F) UV–Vis-NIR absorption spectra of ICG, $AlCl_3$, LS, and LS-Al-ICG. (G) Molecular docking and (H) binding energy of LS + ICG and LS-Al-ICG. (I) Photothermal images of LS-Al-ICG at different concentrations of ICG and (J) corresponding temperature curves (808 nm, 1 W/cm^2, 5 min). (K) Drug releasing profile of ICG from LS-Al-ICG at pH 5.0, 6.2 or 7.4.

Computational simulations by molecular docking were conducted to further clarify the self-assembly mechanism [41]. As shown in Fig. 2G, Al^{3+} was predicted to play a critical role in self-assembly process. No self-assembly occurred without Al^{3+} due to insufficient molecular interactions between LS and ICG in terms of π–π stacking and hydrophobic interactions. In contrast, when Al^{3+} is present, it can act as a bridging unit to facilitate the self-assembly process by forming coordination bonds of 3.0 and 3.1 Å in length with the sulfonate groups of LS and ICG, respectively. These interactions induce the formation of a hydrogen bond (2.1 Å in length) between the sulfonate group of LS and the hydroxyl group of ICG. In addition, the self-assembled LS-Al-ICG system was stable owing to the higher binding energy of LS-Al-ICG (−2.84 eV) than that of LS + ICG (−1.88 eV) (Fig. 2H).

To further explore the photothermal potential of LS-Al-ICG, we monitored and recorded their thermal images and the corresponding photothermal-heating curves. As displayed in Fig. 2I-2J, the temperature of pure water did not change noticeably following 808 nm laser irradiation, while LS-Al-ICG displayed a dose-dependent temperature elevation, suggesting efficient photothermal conversion of LS-Al-ICG. Free ICG was significantly photolyzed during the third irradiation-cooling cycle, while the temperature of LS-Al-ICG did not change significantly during five irradiation-cooling cycles, suggesting the significant photostability of LS-Al-ICG (Fig. S8). Notably, the photothermal conversion efficiency (η) of LS-Al-ICG was calculated to be 37.85% (Fig. S9), which is higher than free ICG (22.39%) [42]. The enhanced photostability and photothermal conversion of LS-Al-ICG may be related to supramolecular nanostructures [43].

The drug releasing profile was evlauated with a dialysis-based approach (Fig. 2K). After 24 h, 9.14% of ICG was cumulatively released at pH 7.4, which increased significantly to 12.95% or 33.67% at pH 6.2 or 5.0, respectively. Thus, ICG exhibited a pH-sensitive release behavior, which should be

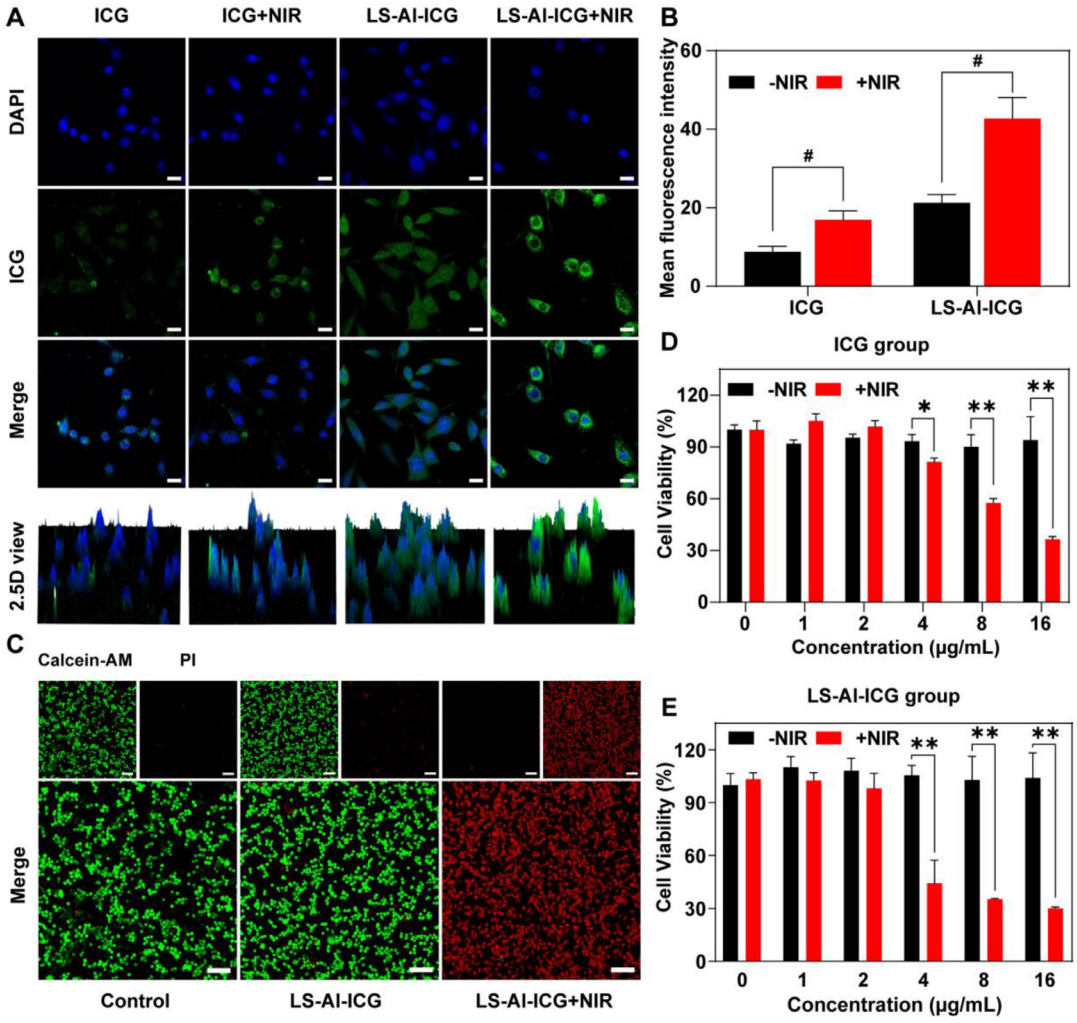

Fig. 3 – *In vitro* cellular uptake and cytotoxicity study. (A) CLSM images and (B) the corresponding mean fluorescence quantification of 4T1 cells treated with ICG or LS-Al-ICG. Scale bar: 20 μm. (C) Live/dead staining assay after different treatments. Scale bar: 100 μm. (D-E) Cell viability of 4T1 cells incubated with ICG and LS-Al-ICG at different concentrations. ($n = 6$, mean ± SD, *$P < 0.05$, **$P < 0.01$ and #$P < 0.0001$).

ascribed to protonation of the sulfonate group that weakened the coordination effect and hydrogen bond [44].

3.2. *In vitro cellular uptake, cytotoxicity, and immunostimulatory activity*

The cellular uptake of ICG and LS-Al-ICG *in vitro* was examined in 4T1 tumor cells by CLSM. As presented in Fig. 3A-3B, unlike free ICG, LS-Al-ICG was readily internalized into 4T1 cells, simultaneously, the laser irradiation significantly increased the cellular uptake of LS-Al-ICG, as evidenced by 2.01-fold higher intracellular fluorescence intensity in the LS-Al-ICG + NIR group than in the LS-Al-ICG group, implying that the increased cellular uptake of LS-Al-ICG was caused by NIR. According to reports, the photothermal effect can cause increased membrane permeability and fluidity, which contributes to enhanced cellular uptake and causes severe damage to the cells [45].

Motivated by the photothermal properties and effective cellular uptake by 4T1 cells, we determined the cytotoxicity of ICG and LS-Al-ICG in 4T1 cancer cells *via* CCK-8 assays to validate the *in vitro* tumor ablating efficiency mediated by photothermal effect. The cell-viability assays revealed a remarkable dose-dependent decrease upon treatment with ICG or LS-Al-ICG and exposure to NIR laser irradiation, and the antitumor effect of LS-Al-ICG was greater than that of ICG (Fig. 3D-3E). Nevertheless, the viability of 4T1 cells and HUVEC remained above 90% without laser irradiation, indicating that LS-Al-ICG has low toxicity and good biocompatibility (Fig S10). Moreover, co-staining was conducted with calcein-AM and PI to verify the therapeutic efficacy, where the green fluorescence and red fluorescence are regarded as an indicator of living cells and dead cells, respectively. As shown in Fig. 3C, LS-Al-ICG treatment demonstrated no noticeable cytotoxicity to 4T1 cells without laser irradiation reflected by the solid green fluorescence. In contrast, intense red fluorescence was

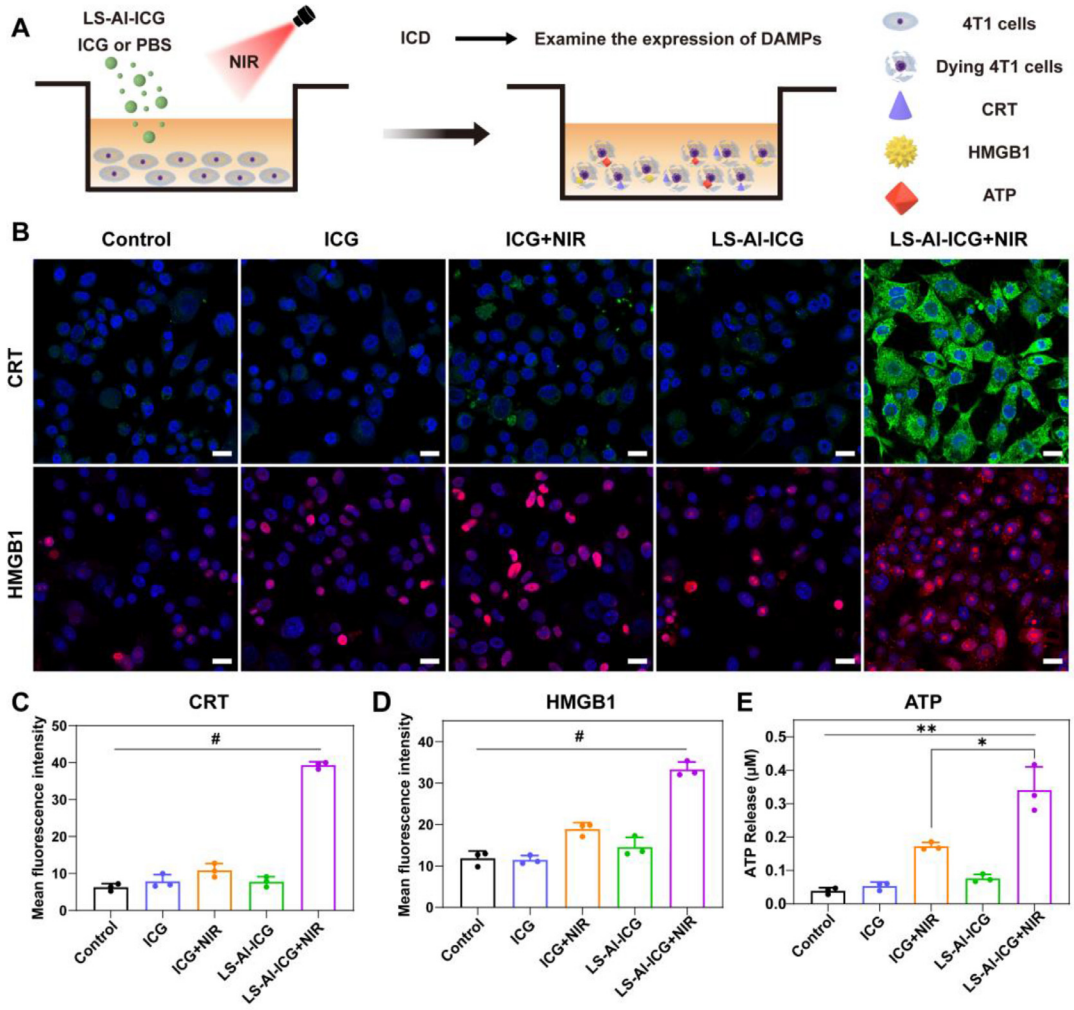

Fig. 4 – *In vitro* DAMPs evaluation. (A) Image illustrating the design of the DAMPs evaluation experiments. (B) CLSM examinations of CRT and HMGB1 release in LS-AI-ICG treated 4T1 cells. Scale bar: 20 μm. (C-D) Quantification of mean fluorescence intensity by imageJ according to (B). (E) The ATP secretion in LS-AI-ICG-treated 4T1 cells. ($n = 3$, mean ± SD, *$P < 0.05$, **$P < 0.01$ and #$P < 0.0001$).

observed upon laser irradiation, indicating that LS-AI-ICG can photothermally ablating tumor cells with high efficiency.

To explore the mechanism underlying the superior anti-tumor efficacy of LS-AI-ICG, we investigated PTT-induced ICD generation and DCs maturation *in vitro*. Typical DAMPs of ICD include CRT translocation to the cell surface, HMGB1 expression, and ATP release. These features can promote tumor antigen phagocytosis and presentation by DCs, thereby facilitating the production of CTLs [9,17,46-48]. The expression levels of DAMPs on 4T1 cells *in vitro* after different treatments were examined using CLSM and flow cytometric measurements (Fig. 4A). The immunofluorescence-staining images showed that, compared to the moderate upregulation of CRT and HMGB1 in the ICG + NIR group, after laser irradiation of 4T1 cells incubated with LS-AI-ICG, intense green and red fluorescent signals could be detected from CRT and HMGB1, suggesting that the cytoplasmic levels of CRT and HMGB1 increased markedly (Fig. 4B). In the LS-AI-ICG + NIR group, the mean fluorescence intensities for CRT and HMGB1 staining were significantly stronger than those in the ICG + NIR group (approximately 6.0- and 2.5-fold higher than those in the control group, respectively; Fig. 4C-4D). Moreover, the ATP level in the LS-AI-ICG + NIR treatment group was almost 3.0-fold of that in the ICG + NIR group, whereas the ICG group and the LS-AI-ICG group did not show obvious differences when compared with the control group (Fig. 4E). In summary, LS-AI-ICG-mediated PTT dramatically elicited ICD in 4T1 cells and triggered an anti-tumor immune response.

DCs are one of the most important APCs, playing critical roles in immune responses. DAMPs released by dying tumor cells during ICD can stimulate DCs maturation and further activate immune responses [7,26,49]. Therefore, we studied the *in vitro* stimulatory effects on BMDCs induced by various treatments (Fig. 5A). After 24-h incubation with corresponding 4T1 cell culture supernatants, BMDCs harvested from BALB/c mice were subjected to flow cytometry for analyzing the expression of $CD80^+$ and $CD86^+$ of $CD11c^+$ DCs. We found that 4T1 cells treated with LS-AI-ICG + NIR displayed a much more significant increase in DCs maturity than the

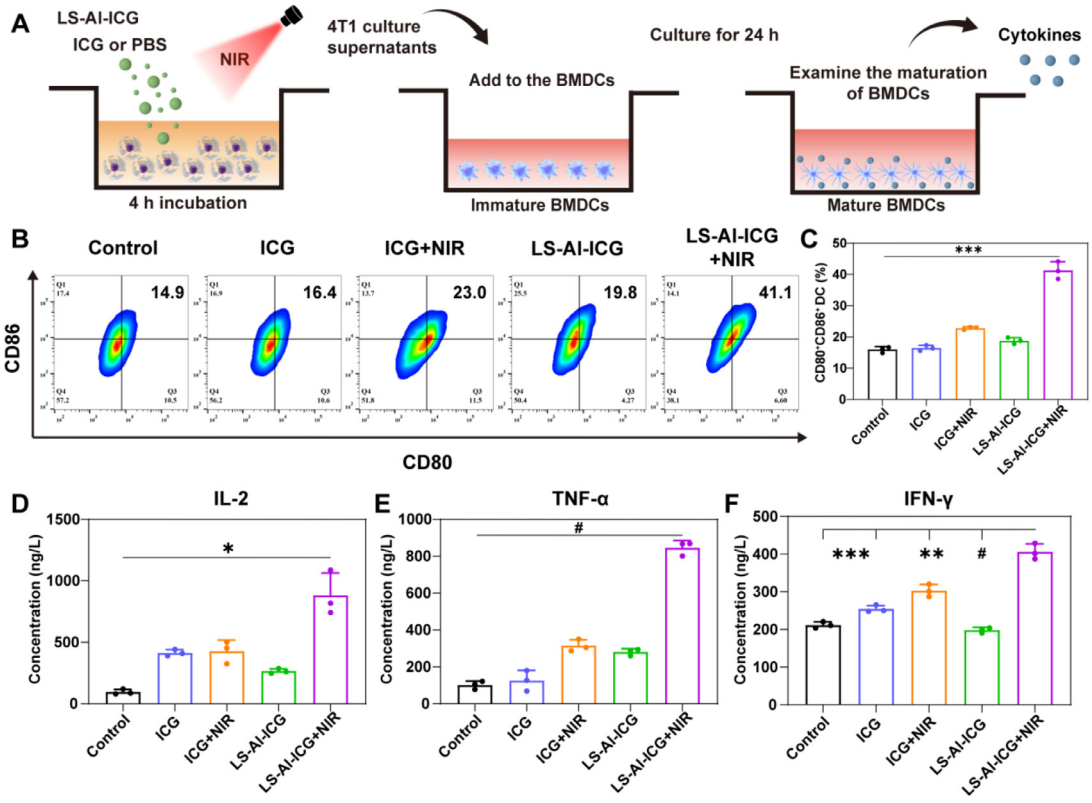

Fig. 5 – *In vitro* dendritic cells maturation. (A) Image illustrating the design of DCs maturation process. (B) Flow cytometry assay of the expression level of $CD80^+$ and $CD86^+$gated on $CD11c^+$ in BMDCs after different treatments. (C) Quantitative percentages of $CD80^+CD86^+$ DCs gated on $CD11c^+$ DCs according to (B). (D-F) Secretion of IL-2, TNF-α and IFN-γ from the BMDCs was determined by ELISA. ($n = 3$, mean ± SD, *P < 0.05, **P < 0.01, ***P < 0.001 and #P < 0.0001).

ICG + NIR and control groups (Fig. 5B-5C). In contrast, free ICG and LS-Al-ICG exhibited a negligible stimulatory effect on DCs maturation without NIR irradiation. These results demonstrated that LS-Al-ICG + NIR efficiently induced DCs maturation. The secretion levels of cytokines related to DCs activation (IL-2, TNF-α, and IFN-γ; important markers of cellular immunity) in the culture supernatants were recorded to assess immunoactivation [50]. Fig. 5D-5F reveal that the LS-Al-ICG + NIR group displayed the highest secretion of IL-2, TNF-α, and IFN-γ. These findings indicate that the ICD of cancer cells promotes DCs maturation through PTT and aluminum adjuvants, which is vital for subsequent tumor immunotherapy of T cell.

3.3. *Biodistribution and photothermal imaging of LS-AL-ICG in vivo*

ICG and LS-Al-ICG were injected intravenously into 4T1 tumor-bearing mice to monitor the biodistribution. As shown in Fig. 6A, after administering ICG and LS-Al-ICG, intense fluorescence signals were observed throughout the whole body. ICG fluorescence was barely detectable in mice administrated with ICG alone at 8 h post-administration, suggesting rapid clearance of free ICG molecules. However, the LS-Al-ICG exhibited significant fluorescence at tumor sites for over 24 h, demonstrating a prolonged circulation time and enhanced tumor accumulation (Fig. 6B). As determined in Fig. 6C, results indicated anticipated clearance of the supramolecular self-assembly through the reticuloendothelial system (RES) as marked by LS-Al-ICG accumulation in liver, spleen, lung, and kidney [51]. Generally, NPs smaller than 10 nm are swiftly filtered and excreted by the kidneys, showing excellent *in vivo* safety [52]. However, because of the ability to extravasate leaky tumor blood vessels, LS-Al-ICG (<10 nm) may show higher opportunity of the rapid drug accumulation and deep penetration [53]. Nevertheless, the fluorescence intensity of mice was weaker in the ICG group, further indicating that free ICG was completely cleared. The semi-quantitative analysis shown in Fig. 6D indicated that the average intratumoral fluorescence intensity of LS-Al-ICG was 5.7 times higher than that of free ICG, suggesting that LS-Al-ICG had excellent performance in terms of tumor accumulation [38].

In vivo fluorescence experiments showed that NPs accumulation peaked at approximately 0.75 h after administration. *In vivo* photothermal treatment was conducted considering that LS-Al-ICG may degrade at the tumor sites. At 4 h after intravenously injecting mice with saline, ICG, or LS-Al-ICG, their primary tumors were subjected to 808 nm irradiation (5 min, 1 W/cm^2). Then, the temperatures of the tumor regions in LS-Al-ICG-injected mice gradually increased and peaked at approximately 52 °C after 5 min (Fig. 6E-6F). In contrast, the temperatures of the tumor regions of ICG-treated mice increased inconspicuously

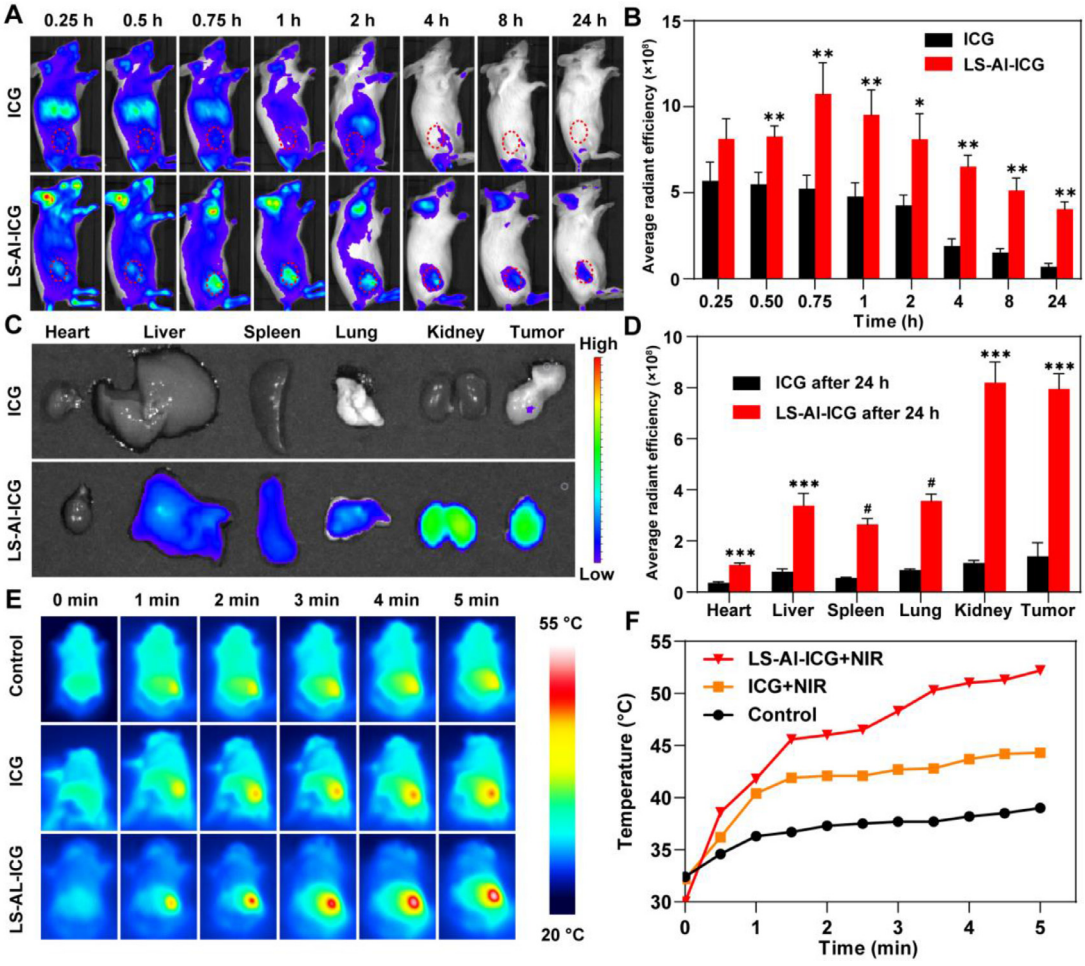

Fig. 6 – *In vivo* biodistribution and photothermal evaluation. (A) Fluorescence images of ICG and LS-Al-ICG injection. (B) Semi-quantitative fluorescence intensity at the primary tumor sites after different treatments. (C) *Ex vivo* fluorescence images of major organs and tumors at 24 h after injection. (D) *Ex vivo* fluorescence intensity of ICG or LS-Al-ICG. (E) Thermal images and (F) temperature curve at 0, 1, 2, 3, 4, and 5 min at 4 h after various injection. ($n = 3$, mean ± SD, *$P < 0.05$, **$P < 0.01$, ***$P < 0.001$ and #$P < 0.0001$).

following irradiation due to insufficient ICG accumulation in the tumors.

3.4. *In vivo anti-tumor effects*

A dual-4T1 tumor model was established to evaluate the anticancer efficacy of PTT mediated by NIR laser irradiation and immunotherapy mediated through an aluminum adjuvant and PD-1 blocking [50,54]. The 4T1 tumor-bearing mice were randomly divided into six groups: the control group, ICG group, ICG + NIR group, LS-Al-ICG group, LS-Al-ICG + NIR group, and LS-Al-ICG + NIR + anti-PD-1 group. Only the primary tumors were treated after tail vein administration, whereas distant tumors showed natural growth (Fig. 7A). As shown in Fig. 7B and Fig. 7E, with the implementation of irradiation and PD-1 blockade, a remarkable growth inhibitory effect on primary tumors was observed. What is more, similar results were also observed regarding the volumes of distant tumors, implying that an abscopal effect occurred (Fig. 7C). The distant tumor volumes of the ICG + NIR group were slightly smaller than those of the control, ICG, and LS-Al-ICG groups, which shall be ascribed to the slight ICG mediated ICD-activity for immune response. In contrast, the distant tumor volumes in the LS-Al-ICG + NIR group and the LS-Al-ICG + NIR + anti-PD-1 group were significantly smaller than those in the ICG + NIR group ($P < 0.05$). This distinctly improved therapeutic efficacy could be attributed to PTT-induced immune responses. Greater changes in the tumor volumes were observed in the LS-Al-ICG + NIR + anti-PD-1 group than in the LS-Al-ICG + NIR group, due to the inclusion of the anti-PD-1 antibody. These observations indicated that PTT plus modulation of the tumor microenvironment induced by LS-Al-ICG and PD-1 blockade can dramatically improve the treatment efficacy and suppress both primary and distant tumors.

In addition, mice in the LS-Al-ICG + NIR group and LS-Al-ICG + NIR + anti-PD-1 group exhibited significantly prolonged survival period. Approximately 80% and 60% of the mice survived during the 50-d observation period, respectively, in marked contrast to the mice in the other groups, all of

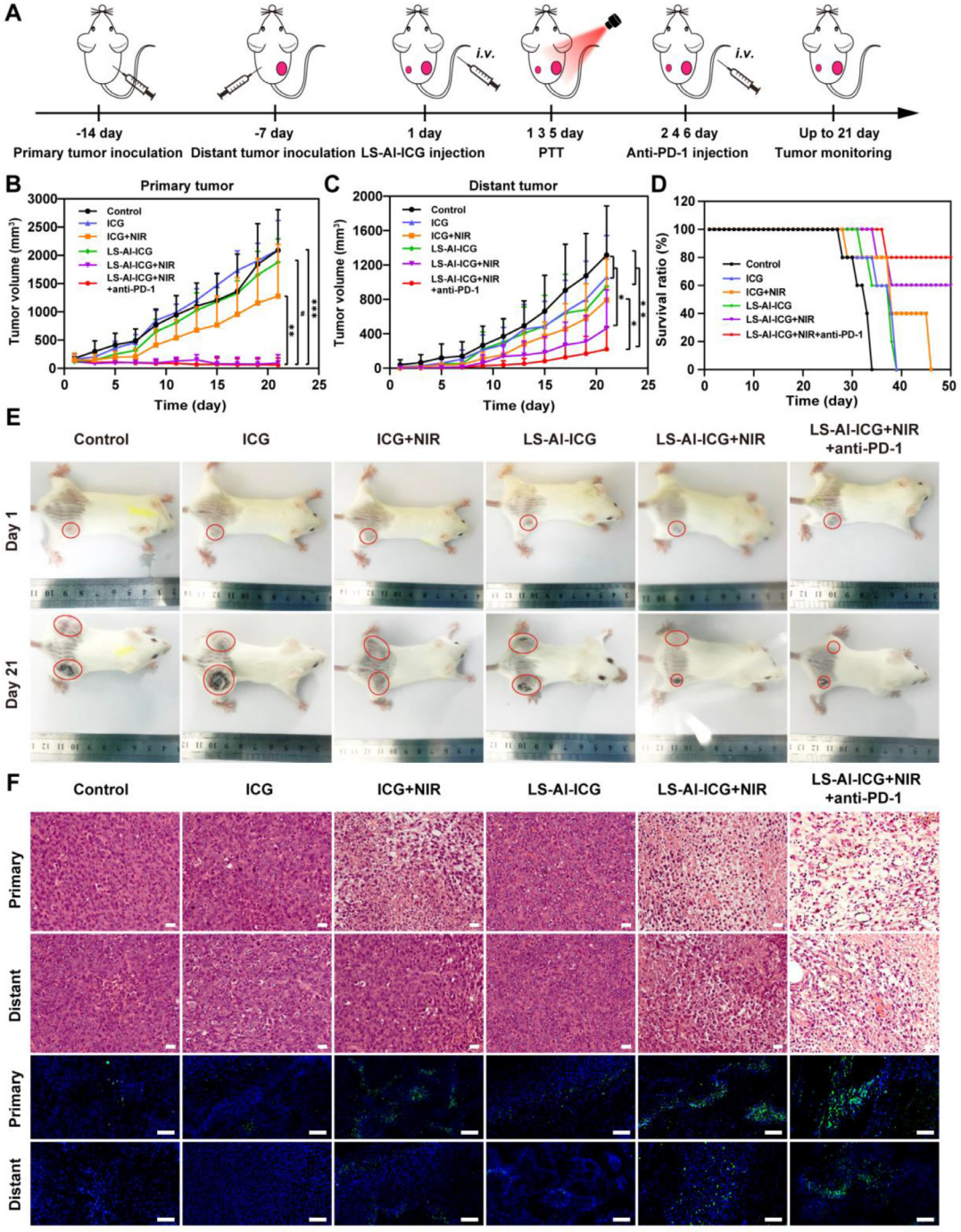

Fig. 7 – *In vivo* anti-tumor effects. (A) Protocol for pharmacodynamic modeling and treatment. (B-D) Relative primary tumor volume, distant tumor volume, and survival ratio after different treatments. (E) Photographs of mice at 1st and 21th day. Bilateral tumor sites were marked with red circles. (F) H&E and TUNEL staining of bilateral tumor tissue sections after different treatment methods. Scale bar: 100 μm ($n = 5$, mean ± SD, *$P < 0.05$, **$P < 0.01$, ***$P < 0.001$ and #$P < 0.0001$).

which died between 34 and 39 d (Fig. 7D). Furthermore, no significant abnormalities were observed in the mouse body weights (Fig. S11), suggesting excellent biocompatibility. H&E and TUNEL staining results of primary and distant tumor sections revealed significantly more necrosis and apoptosis in tumor tissue samples from the LS-Al-ICG + NIR + anti-PD-1 group and the LS-Al-ICG + NIR group than in those from the other groups, which was consistent with *in vivo* antitumor outcomes (Fig. 7F).

Major organs were then harvested for pathological analysis. In contrast to the control group, no obvious tissue damage or inflammatory responses were observed by H&E staining in any sections from the treatment groups, which indicated the excellent biocompatibility of LS-Al-ICG

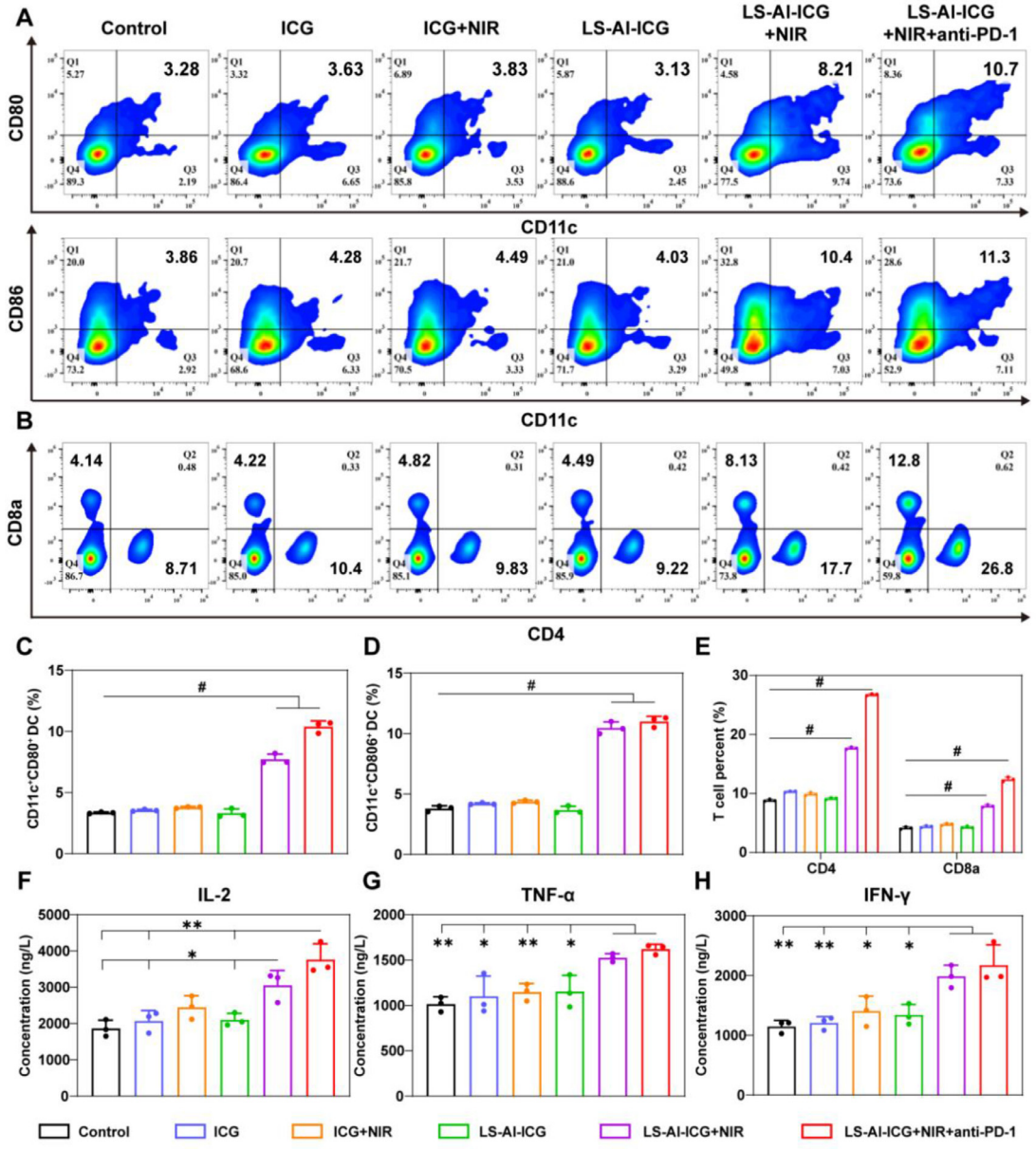

Fig. 8 – *In vivo* immune responses assessment. (A) Flow cytometry assay of CD80$^+$ or CD86$^+$ gated on CD11c$^+$ in the TDLNs of mice. (B) Flow cytometry assay illustrated the percent of CD8a$^+$ T cells and CD4$^+$ T cells gated on CD3$^+$ T cells in splenocytes of mice. (C-D) Quantitative percentages of CD80$^+$ or CD86$^+$ expressions gated on CD11c$^+$ according to (A). (E) Quantitative percentages of CD8a$^+$ T cells and CD4$^+$ T cells in splenocytes according to (B). (F-H) Quantitative analysis of the immune-associated cytokines in serum, as determined by ELISA (IL-2, TNF-α and IFN-γ). ($n = 3$, mean ± SD, *P < 0.05, **P < 0.01 and ##P < 0.0001).

(Fig. S12). The biocompatibility of the metal-coordinated, supramolecular, self-assembled nanosystem was ascribed to the NP composition (nontoxic LS self-assembled with aluminum ion and ICG in water, without any toxic substances or organic solvents).

3.5. *Assessment of immune activation in vivo*

PTT is capable of killing cancer cells and promoting tumor-specific immune responses. Hence, we predicted that LS-Al-ICG, combined with PTT and anti-PD-1 therapy, could effectively activate immune responses *in vivo* [49,55-57]. Seven days after different treatments with the dual-4T1 tumor-bearing mice, we investigated DCs activation in TDLNs and primary tumors, the proportion of T lymphocytes in splenocytes, and several key serum cytokine levels.

Combination treatment with PTT based on LS-Al-ICG and immunotherapy with anti-PD-1 can significantly increase the expression of CD80$^+$ or CD86$^+$ within TDLN (Fig. 8A, 8C-8D). These results suggest that combination therapy-induced DCs maturation through the effects of aluminum adjuvants and the PD-1 antibody. As expected, DCs from the LS-Al-ICG + NIR

group showed higher expression levels of costimulators than DCs from the ICG + NIR group, with 8.20% *versus* 3.83% $CD11c^+CD80^+$ cells and 10.4% *versus* 4.49% $CD11c^+CD86^+$ cells, respectively. These findings were attributed to the fact that aluminum adjuvants enhance immune responses by enhancing antigen phagocytosis and processing APCs. In addition, similar DCs-maturation levels were observed in the primary tumors, and the differences were less significant compared to those in DCs from the lymph nodes (Fig. S13).

CTLs and helper T cells play prominent roles in anti-tumor immune responses by releasing cytotoxins and regulating adaptive immunity, respectively. Single-cell suspensions were prepared from mouse spleens, which were evaluated to study the immune responses induced by LS-Al-ICG. The abundances of $CD4^+$ and $CD8^+$ T cells were detected by flow cytometry (Fig. 8B). Our results showed that different alum forms (such as aluminum hydroxide and aluminum phosphate) stimulated humoral immunity with limited effects on $CD8^+$ T cells [26]. However, co-delivering an aluminum adjuvant with the photosensitizer ICG triggered strong cellular immunity. The LS-Al-ICG + NIR group showed significantly elevated percentages of $CD4^+$ and $CD8^+$ T cells in spleen, whereas treatment with free ICG (with or without NIR and LS-Al-ICG) failed to increase the abundances of $CD4^+$ and $CD8^+$ T cells. Notably, combined treatment with LS-Al-ICG and anti-PD-1 blockade increased populations of $CD4^+$ and $CD8^+$ T cells, which could explain the priming immunity and remodeling of immunosuppressive tumor microenvironment (Fig. 8E).

Further, anti-tumor cytokine levels in serum (IL-2, TNF-α, and IFN-γ) of mice were measured. As displayed in Fig. 8F-8H, compared with the control group, these cytokine levels were only increased slightly in the ICG + NIR group, indicating that treatment with free ICG and NIR irradiation had a limited stimulatory effect on the immune response *in vivo*. In contrast, these cytokine levels in the LS-Al-ICG + NIR group and LS-Al-ICG + NIR + anti-PD-1 group were significantly higher. The higher cytokine levels of the LS-Al-ICG + NIR + anti-PD-1 group (as compared to those of LS-Al-ICG + NIR group) showed that the immune-checkpoint inhibitor enhanced the immune response.

4. Conclusions

In summary, we developed a simple strategy for co-delivering ICG and an aluminum adjuvant using LS as an indispensable accessory for cancer photothermal immunotherapy. Lignin-assisted construction of a sub-10 nm, supramolecular self-assembling nanosystem is exceptionally promising for bridging the superiority between aluminum adjuvants and ICG. Our *in vitro* results demonstrated that administering LS-Al-ICG with NIR irradiation efficiently enhanced cellular uptake and cytotoxicity in 4T1 cells. Moreover, maximum ICD promoted BMDCs maturation by increasing the expression levels of DAMPs and immune-associated cytokines. After tail vein injection, LS-Al-ICG exhibited high aggregation at tumor sites, which led to an excellent photothermal-conversion effect. Anti-PD-1 therapy, when combined with LS-Al-ICG treatment, triggered the maturation of DCs, which recruited and activated CTLs for synergized immunotherapy against primary and distant breast tumors *in vivo*. This low-cost and facile strategy provides a feasible regimen for combining PTT and immunotherapy and serves as a paradigm to show the promise of naturally derived LS as a biomaterial for oncotherapy.

Conflicts of interest

The authors report no conflicts of interest.

Acknowledgments

This study was financially supported by the National Natural Science Foundation of China (No. 82074027, No. 81873014, No. 82104405, No. 81873018, No.82174096), Natural Science Foundation of Zhejiang Province (No. LZ21H280001). We appreciate the great help from the Public Platform of Medical Research Center, Academy of Chinese Medical Sciences, Zhejiang Chinese Medical University.

Supplementary materials

Supplementary material associated with this article can be found, in the online version, at doi:10.1016/j.ajps.2022.07.002.

REFERENCES

[1] Li B, Hao G, Sun B, Gu Z, Xu Z. Engineering a therapy-induced "Immunogenic cancer cell death" amplifier to boost systemic tumor elimination. Adv Funct Mater 2020;30(22):1909745.
[2] Zhou L, Zhang P, Wang H, Wang D, Li Y. Smart nanosized drug delivery systems inducing immunogenic cell death for combination with cancer immunotherapy. Acc Chem Res 2020;53(9):1761–72.
[3] Deng C, Zhang Q, Jia M, Zhao J, Sun X, Gong T, et al. Tumors and their microenvironment dual-targeting chemotherapy with local immune adjuvant therapy for effective antitumor immunity against breast cancer. Adv Sci 2019;6(6):1801868.
[4] Huang X, Lu Y, Guo M, Du S, Han N. Recent strategies for nano-based PTT combined with immunotherapy: from a biomaterial point of view. Theranostics 2021;11(15):7546–69.
[5] Chen X, Zou J, Zhang K, Zhu J, Zhang Y, Zhu Z, et al. Photothermal/matrix metalloproteinase-2 dual-responsive gelatin nanoparticles for breast cancer treatment. Acta Pharm Sin B 2021;11(1):271–82.
[6] Piao J, Wang L, Gao F, You Y, Xiong Y, Yang L. Erythrocyte membrane is an alternative coating to polyethylene glycol for prolonging the circulation lifetime of gold nanocages for photothermal therapy. ACS Nano 2014;8(10):10414–25.
[7] Huang R, Ding Z, Jiang B, Luo Z, Chen T, Guo Z, et al. Artificial metalloprotein nanoanalogues: *in situ* catalytic production of oxygen to enhance photoimmunotherapeutic inhibition of primary and abscopal tumor growth. Small 2020;16(46):2004345.
[8] Jin F, Qi J, Zhu M, Liu D, You Y, Shu G, et al. NIR-triggered sequentially responsive nanocarriers amplified cascade synergistic effect of chemo-photodynamic therapy with

inspired antitumor immunity. ACS Appl Mater Interfaces 2020;12(29):32372–87.
[9] Li J, Yu X, Jiang Y, He S, Zhang Y, Luo Y, et al. Second near-infrared photothermal semiconducting polymer nanoadjuvant for enhanced cancer immunotherapy. Adv Mater 2020;33(4):2003458.
[10] Noh I, Son Y, Jung W, Kim M, Kim D, Shin H, et al. Targeting the tumor microenvironment with amphiphilic near-infrared cyanine nanoparticles for potentiated photothermal immunotherapy. Biomaterials 2021;275:120926.
[11] Chen Z, Liu L, Liang R, Luo Z, He H, Wu Z, et al. Bioinspired hybrid protein oxygen nanocarrier amplified photodynamic therapy for eliciting anti-tumor immunity and abscopal effect. ACS Nano 2018;12(8):8633–45.
[12] Wan S, Zhang B, Li S, He B, Pu Y. Combination of PEG-decorated black phosphorus nanosheets and immunoadjuvant for photoimmunotherapy of melanoma. J Mat Chem B 2020;8(14):2805–13.
[13] Hameed S, Mo S, Mustafa G, Bajwa S, Khan W, Dai Z. Immunological consequences of nanoparticle-mediated antitumor photoimmunotherapy. Adv Ther 2020;3(5):1900101.
[14] Duan X, Chan C, Lin W. Nanoparticle-mediated immunogenic cell death enables and potentiates cancer immunotherapy. Angew Chem Int Edit 2019;58(3):670–80.
[15] Banstola A, Jeong J, Yook S. Immunoadjuvants for cancer immunotherapy: a review of recent developments. Acta Biomater 2020;114:16–30.
[16] Lim S, Park J, Shim M, Um W, Yoon H, Ryu J, et al. Recent advances and challenges of repurposing nanoparticle-based drug delivery systems to enhance cancer immunotherapy. Theranostics 2019;9(25):7906–23.
[17] Ding B, Zheng P, Jiang F, Zhao Y, Wang M, Chang M, et al. MnO(x)nanospikes as nanoadjuvants and immunogenic cell death drugs with enhanced antitumor immunity and antimetastatic effect. Angew Chem Int Edit 2020;59(38):16381–4.
[18] Zhang F, Lu G, Wen X, Li F, Ji X, Li Q, et al. Magnetic nanoparticles coated with polyphenols for spatio-temporally controlled cancer photothermal/immunotherapy. J Controlled Release 2020;326:131–9.
[19] Chen Q, Xu L, Liang C, Wang C, Peng R, Liu Z. Photothermal therapy with immune-adjuvant nanoparticles together with checkpoint blockade for effective cancer immunotherapy. Nat Commun 2016;7:13193.
[20] Hu W, Xiao T, Li D, Fan Y, Xing L, Wang X, et al. Intelligent molybdenum disulfide complexes as a platform for cooperative imaging-guided tri-dode chemo-photothermo-immunotherapy. Adv Sci 2021;8(14):2100165.
[21] Wang N, Zhang G, Sun H, Tian Y, Hao J, Cui J. Vaccine nanoparticles derived from mung beans for cancer immunotherapy. Chem Mater 2021;33(11):4057–66.
[22] Moyer T, Kato Y, Abraham W, Chang J, Kulp D, Watson N, et al. Engineered immunogen binding to alum adjuvant enhances humoral immunity. Nat Med 2020;26(3):430–40.
[23] HogenEsch H. Mechanism of immunopotentiation and safety of aluminum adjuvants. Front Immunol 2013;3:406.
[24] Goldberg M. Improving cancer immunotherapy through nanotechnology. Nat Rev Cancer 2019;19(10):587–602.
[25] Chen W, Qin M, Chen X, Wang Q, Zhang Z, Sun X. Combining photothermal therapy and immunotherapy against melanoma by polydopamine-coated Al_2O_3 nanoparticles. Theranostics 2018;8(8):2229–41.
[26] Zhu Y, Xue J, Chen W, Bai S, Zheng T, He C, et al. Albumin-biomineralized nanoparticles to synergize phototherapy and immunotherapy against melanoma. J Controlled Release 2020;322:300–11.
[27] Cabral H, Kinoh H, Kataoka K. Tumor-targeted nanomedicine for immunotherapy. Acc Chem Res 2020;53(12):2765–76.
[28] Chang M, Wang M, Wang M, Shu M, Ding B, Li C, et al. A multifunctional cascade bioreactor based on hollowstructured Cu_2MoS_4 for synergetic cancer chemo-dynamic therapy/starvation therapy/phototherapy/immunotherapy with remarkably enhanced efficacy. Adv Mater 2019;31(51):1905271.
[29] Xu J, Wang J, Ye J, Jiao J, Liu Z, Zhao C, et al. Metal-coordinated supramolecular self-assemblies for cancer theranostics. Adv Sci 2020;8(16):2101101.
[30] Zhang Y, Ma S, Liu X, Xu Y, Zhao J, Si X, et al. Supramolecular assembled programmable nanomedicine as *in situ* cancer vaccine for cancer immunotherapy. Adv Mater 2021;33(7):2007293.
[31] Yang Y, Zhu W, Dong Z, Chao Y, Xu L, Chen M, et al. 1D coordination polymer nanofibers for low-temperature photothermal therapy. Adv Mater 2017;29(40):1703588.
[32] Ganewatta M, Lokupitiya H, Tang C. Lignin biopolymers in the age of controlled polymerization. Polymers (Basel) 2019;11(7):1176.
[33] Wang J, Zhang D, Chu F. Wood-derived functional polymeric materials. Adv Mater 2020;33(28):2001135.
[34] Iravani S, Varma R. Greener synthesis of lignin nanoparticles and their applications. Green Chem 2020;22:612–36.
[35] Etman S, Abdallah O, Mehanna R, Elnaggar Y. Lactoferrin/Hyaluronic acid double-coated lignosulfonate nanoparticles of quinacrine as a controlled release biodegradable nanomedicine targeting pancreatic cancer. Int J Pharm 2020;578:119097.
[36] Bao D, Xie Y, Ma S, Wu Z, Piao J. Self-assembly of a renewable lignin biopolymer in nanoparticles with multiple morphologies. J Appl Polym Sci 2019;136:47482.
[37] Zou J, Bao D, Ma R, Zhu Z, Chen X, Zhu J, et al. Green and sustainable self-assembly nanocomposite from gentamicin sulfate/lignosulfonate with efficient antibacterial and wound-healing activity. ACS Sustainable Chem Eng 2020;8(12):4931–40.
[38] Feng B, Niu Z, Hou B, Zhou L, Li Y, Yu H. Enhancing triple negative breast cancer immunotherapy by ICG-templated self-assembly of paclitaxel nanoparticles. Adv Funct Mater 2020;30(6):1906605.
[39] An H, Li L, Wang Y, Wang Z, Hou D, Lin Y, et al. A tumour-selective cascade activatable self-detained system for drug delivery and cancer imaging. Nat Commun 2019;10:4861.
[40] Sun H, Liu D, Du J. Nanobowls with controlled openings and interior holes driven by the synergy of hydrogen bonding and π-π interaction. Chem Sci 2019;10(3):657–64.
[41] Huang L, Chen X, Bian Q, Zhang F, Wu H, Wang H, et al. Photosensitizer-stabilized self-assembling nanoparticles potentiate chemo/photodynamic efficacy of patient-derived melanoma. J Controlled Release 2020;328:325–38.
[42] Qi J, Xiong Y, Cheng K, Huang Q, Cao J, He F, et al. Heterobifunctional PEG-grafted black phosphorus quantum dots: “three-in-one” nanoplatforms for mitochondria-targeted photothermal cancer therapy. Asian J Pharm Sci 2021;16(2):222–35.
[43] Zhao L, Liu Y, Xing R, Yan X. Supramolecular photothermal effects: a promising mechanism for efficient thermal conversion. Angew Chem Int Edit 2020;59(10):3793–801.
[44] Chen B, Kankala R, He G, Yang D, Li G, Wang P, et al. Supercritical fluid-assisted fabrication of indocyanine green-encapsulated silk fibroin nanoparticles for

dual-triggered cancer therapy. ACS Biomater Sci Eng 2018;4(10):3487–97.
[45] Shao J, Liang R, Ding D, Zheng X, Zhu X, Hu S, et al. A smart multifunctional nanoparticle for enhanced near-infrared image-guided photothermal therapy against gastric cancer. Int J Nanomed 2021;16:2897–915.
[46] Zhao L, Zheng R, Huang J, Chen X, Deng F, Liu Y, et al. Self-delivery photo-immune stimulators for photodynamic sensitized tumor immunotherapy. ACS Nano 2020;14(12):17100–13.
[47] Qi J, Li W, Lu K, Jin F, Liu D, Xu X, et al. pH and thermal dual-sensitive nanoparticle-mediated synergistic antitumor effect of immunotherapy and microwave thermotherapy. Nano Lett 2019;19(8):4949–59.
[48] Wen Y, Chen X, Zhu X, Gong Y, Yuan G, Qin X, et al. Photothermal-chemotherapy integrated nanoparticles with tumor microenvironment response enhanced the induction of immunogenic cell death for colorectal cancer efficient treatment. ACS Appl Mater Interfaces 2019;11(46):43393–408.
[49] Wang L, He Y, He T, Liu G, Lin C, Li K, et al. Lymph node-targeted immune-activation mediated by imiquimod-loaded mesoporous polydopamine based-nanocarriers. Biomaterials 2020;255:120208.
[50] Luo L, Yang J, Zhu C, Jiang M, Guo X, Li W, et al. Sustained release of anti-PD-1 peptide for perdurable immunotherapy together with photothermal ablation against primary and distant tumors. J Controlled Release 2018;278:87–99.
[51] Mei X, Ma J, Bai X, Zhang X, Zhang SM, Liang R, et al. A bottom-up synthesis of rare-earth-hydrotalcite monolayer nanosheets toward multimode imaging and synergetic therapy. Chem Sci 2018;9(25):5630–9.
[52] Pan D, Cai X, Yalaz C, Senpan A, Omanakuttan K, Wickline S, et al. Photoacoustic sentinel lymph node imaging with self-assembled copper neodecanoate nanoparticles. ACS Nano 2012;6(2):1260–7.
[53] Huang K, Ma H, Liu J, Huo S, Kumar A, Wei T, et al. Size-dependent localization and penetration of ultrasmall gold nanoparticles in cancer cells, multicellular spheroids, and tumors *in vivo*. ACS Nnao 2012;6(5):4483–93.
[54] Luo L, Zhu C, Yin H, Jiang M, Zhang J, Qin B, et al. Laser immunotherapy in combination with perdurable PD-1 blocking for treatment of metastatic tumor. ACS Nano 2018;12(8):7647–62.
[55] Jia Y, Shi K, Yang F, Liao J, Han R, Yuan L, et al. Multifunctional nanoparticle loaded injectable thermoresponsive hydrogel as NIR controlled release platform for local photothermal immunotherapy to prevent breast cancer postoperative recurrence and metastases. Adv Funct Mater 2020;30:2001059.
[56] Zhao P, Xu Y, Ji W, Zhou S, Li L, Qiu L, et al. Biomimetic black phosphorus quantum dots-based photothermal therapy combined with anti-PD-L1 treatment inhibits recurrence and metastasis in triple-negative breast cancer. J Nanobiotechnol 2021;19(1):181.
[57] Gao A, Chen B, Gao J, Zhou F, Saeed M, Hou B, et al. Sheddable prodrug vesicles combating adaptive immune resistance for improved photodynamic immunotherapy of cancer. Nano Lett 2020;20(1):353–62.